Highly surface-textured and conducting ZnO:Al films fabricated from oxygen-deficient target for Cu(In, Ga)Se_2 solar cell application

Zhou Wang (汪 宙)[1], Dongyun Wan (万冬云)[1], Fuqiang Huang (黄富强)[1*], and Fangfang Xu (许钫钫)[2]

[1]CAS Key Laboratory of Materials for Energy Conversion, Shanghai Institute of Ceramics, Chinese Academy of Sciences, Shanghai 200050, China

[2]Inorganic Materials Analysis and Testing Center, Shanghai Institute of Ceramics, Chinese Academy of Sciences, Shanghai 200050, China

[*]Corresponding author: Huangfq@mail.sic.ac.cn

Received April 29, 2014; accepted June 3, 2014; posted online August 23, 2014

Highly conducting ZnO:Al (AZO) films are normally prepared through substrate heating and post-annealing in reducing atmosphere, which is deleterious to maintain the high transparency of films and the overall solar cell performance. Here we fabricate AZO films through one-step sputtering at room temperature using oxygen-deficient targets prepared via double crucible method. The best-performed AZO film achieves a low resistivity of 4.4×10^{-4} Ω cm, a high haze factor of 35.0%, and optimizes the efficiency of Cu (In, Ga)Se_2 solar cell with a high value of 14.15%. This letter demonstrates that oxygen deficiency can induce high surface texture, conductivity, and boost solar cell performance.

OCIS codes: 000.1570, 040.5350, 160.4670, 240.0310.

doi: 10.3788/COL201412.093101.

ZnO-based transparent conductive oxide (TCO) films have attracted significant attention in the application as a front electrode in solar cells due to the low cost and nontoxicity[1,2]. ZnO:Al (AZO) films have been demonstrated to have high transparency in visible wavelength range and high electrical conductivity, and AZO films are a promising TCO candidate to replace the Sn-doped In_2O_3 films[3] .

In order to obtain high-performance AZO films, the defect manipulation in the films should be placed in the first place. Microstructural defects are the origin of the desired electrical and optical properties[4–7], including visible and infrared light transmittance, electrical conductivity (carrier concentration, carrier mobility), and so on[8,9]. Oxygen vacancies (V_O) is one of the dominant sources of electron carriers in the AZO films. In the conventional methods, the oxygen-deficient AZO films are sputtered with the assistance of substrate heating during sputtering, and the as-sputtered films may be post-annealed in an evacuated or reduced atmosphere[10–12]. Substrate heating and post-annealing (e.g., 200–400 °C[13,14]) are very deleterious to maintain the high transparency of TCO films and the overall performance of solar cells. In the case of Cu (In, Ga)Se_2 (CIGS) thin film solar cells, the pre-formed PN junction can even be destroyed if the front AZO electrodes are sputtered at such high temperature.

In this letter, the home-made oxygen-deficient AZO targets were fabricated via a low-cost double crucible process[15] and further applied in the magnetron sputtering, which realized one-step synthesis for highly conductive and transparent AZO films at room temperature. The oxygen-deficiency state in targets was found benefiting surface-texture behavior in deposited AZO films. This new method, which removed the deleterious post-annealing process at high temperature and provided superior electrical and optical properties, was further investigated in manufacturing the window layer of CIGS thin film solar cell and boosted the cell efficiency.

The AZO targets were prepared by sintering dry-pressed starting materials of ZnO and $Al(OH)_3$ (1 wt% AZO) at 1350 °C for 4 h. The as-sintered targets were subsequently annealed via a double crucible process for 2 h at 800, 900, and 1000 °C, respectively. As illustrated in Fig. 1[15], when heated, the finite oxygen sealed in the up-side-down crucible reacted with graphite and CO was produced, creating a reducing atmosphere in the inner crucible. The oxygen atoms in the grains and on the grain boundaries of ZnO were withdrawn by the reducing atmosphere to generate oxygen-deficient state in the targets.

The AZO films were deposited in a high vacuum magnetron sputtering system (JGP 450) with a base pressure of 2.0×10^{-4} Pa, under a flow of high-purity Ar gas (99.99%, 10 sccm). DC magnetron sputtering was employed to deposit the films on glass slides with a holder target distance of 70 mm. During the sputtering, the pressure was maintained at 0.2 Pa and the sputtering power was 120 W. The film deposited with as-sintered target was labeled as AZO-0 and films deposited with oxygen-deficient target annealed at 800, 900, and 1000 °C were, respectively, labeled as AZO-800, AZO-900, and AZO-1000.

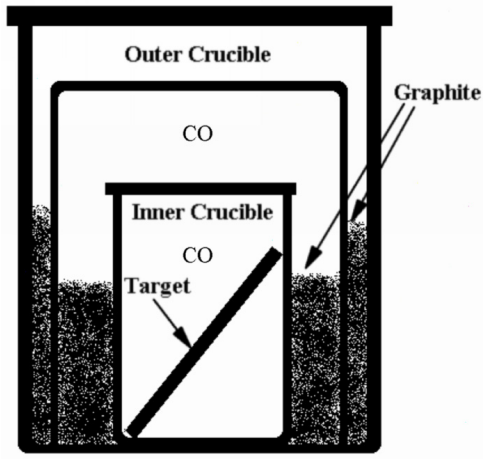

Fig. 1. Schematic diagram of the double crucible annealing method[15].

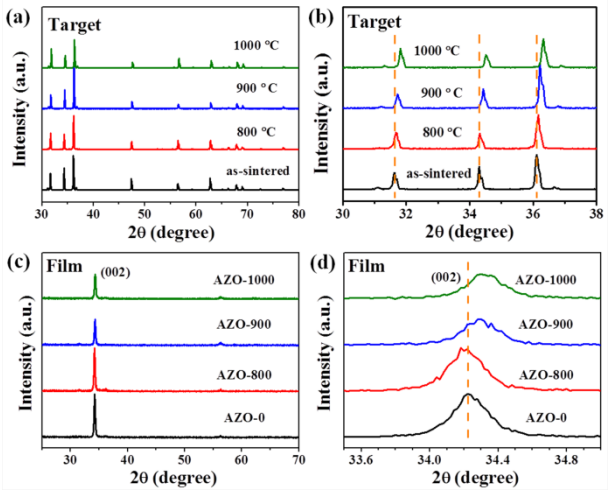

Fig. 2. XRD patterns of (a, b) AZO targets and (c, d) AZO films.

A diffractometer (Advance D8 Focus, Bruker AXS) using Cu-Kα radiation was applied for X-ray diffraction (XRD) measurement to study the crystallization and phase structure of the targets and films. Field emission scanning electron microscopy (FE-SEM; LEO−1530VP), atomic force microscopy (AFM; Seiko II SPI3800V and SPA300HV), and a stylus profiler (Dektak 150, Veeco Instruments) were used to evaluate the surface morphologies, roughness, and thickness of the AZO films. Transmission and haze factor measurements were done on a spectrophotometer (Hitachi U-4100) in the wavelength range of 300−1100 nm. The transmittance spectra reported were obtained after subtraction of signal of glass substrate. The van der Pauw method was used with an Accent HL5500 to measure electrical transport properties including resistivity, carrier concentration, and carrier mobility.

The XRD patterns of the as-sintered and oxygen-deficient AZO targets are shown in Fig. 2. The XRD peaks of all targets are indexed to JCPDS Card No. 36-1451, belonging to the hexagonal wurtzite ZnO. As can be seen in Fig. 2(b), the diffraction peaks of the oxygen-deficient targets shift slightly toward higher angle, which can be ascribed to the lattice contraction caused by oxygen vacancies. The resistance of the 1000 °C-annealed target decreases to less than 1 Ω/sq, much lower than 12 Ω/sq for the as-sintered one. The lower resistance is attributed to higher electron concentration due to more oxygen vacancies formed in the annealing process.

As can be seen Fig. 2(c), all films show the hexagonal wurtzite ZnO structure with evident (0 0 2)-orientated growth perpendicular to the substrate surface. The AZO-0 film exhibits a stronger and sharper peak of (0 0 2), indicating better crystallinity than the films deposited by the oxygen-deficient targets. V_O in the oxygen-deficient targets are demonstrated to hinder the grain crystallization and growth, resulting in smaller grains in the AZO films. Moreover, identical shift toward higher angle can be observed in Fig. 2(d), which is also ascribed to the oxygen-vacancy induced lattice contraction.

The surface morphologies of the AZO films deposited by different targets were evaluated by the distinct AFM topographies, as shown in Fig. 3. All films display randomly distributed "hills" and "valleys," but their size and height distinguish. AZO-0 film exhibits larger but lower hills. With the increasing annealing temperature, the hills become smaller and sharper, which well accords the XRD results. AZO-1000 film finally shows relatively regular array of hills with ~40 nm in height. The evolution of surface morphologies is believed to be ascribed to the intensifying oxygen deficiency during the film growth. During the film growth, atoms reach substrate then face two choices, either participating in the grain growth or nucleation. Normally nucleation requires more energy, which makes it with much lower probability. In the oxygen-deficient films, intensified blocking effect originated from oxygen vacancies increases the energy for participating in growth and hence raises the possibility of nucleation, which hinders the further grain growth and results in smaller "hills". The sharper shape can also be explained by the block effect at grain boundary. The horizontal growth of one

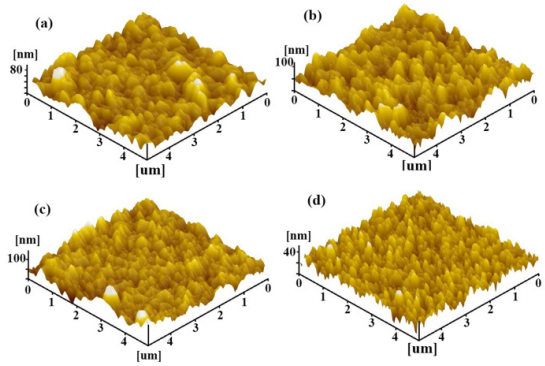

Fig. 3. AFM images of (a) AZO-0, (b) AZO-800, (c) AZO-900, and (d) AZO-1000 films.

Table 1. Structural and Electrical Properties of AZO Films

Sample	**AZO -0**	**AZO -800**	**AZO -900**	**AZO -1000**
RMS Roughness (nm)	11.9	18.3	15.7	6.7
Haze at 360 nm (%)	16.9	35.1	30.8	9.6
ρ (10^{-4} Ωcm)	9.4	4.4	7.3	13.0
μ (cm^2/Vs)	28.3	22.7	9.8	8.3
N (10^{20} cm^{-3})	5.2	6.3	8.8	5.7
Average Transmittance at 400–1100 nm (%)	83.8	86.0	85.7	85.9

grain always needs to compete with neighboring grains. The block effect from grain boundaries of oxygen-deficient films intensified the competition and promotes the vertical growth. As shown in Table 1, the AZO-800 film has the highest root mean square (RMS) roughness of 18.3 nm, compared with 11.9 nm for the AZO-0 film. The low RMS roughness for AZO-1000 (6.7 nm) should be ascribed to the sharply decreased grain size.

The surface and cross-section morphology analyses using FE-SEM obtained identical results with AFM, as shown in Fig. 4. Although the grain size decrease is unobvious, the increased surface roughness for AZO-800 can be distinguished from Fig. 4(b). The cross-section image of AZO-800 film shows typical columnar growth, which is also found in previous reports[16].

Post-annealing AZO films in reducing atmosphere, which is the common method to achieve low resistivity, is usually accompanied with transmittance degeneration. According to the grain-boundary barrier model[17], the potential barrier existing near the grain boundaries is caused by distorted lattice, unsaturated bonds, or impurities. This grain-boundary potential barrier can suppress photon delivery and decrease the transmittance of the film. The optical properties, including transmittance and haze factor, of the AZO films are investigated and shown in Fig. 5. In the optical light region (400—1100 nm), the average transmittance of all the oxygen-deficient AZO films exceeds 85%, as listed in Table 1. The oxygen-deficient films show considerable enhance in transmittance, because the light trapping effect induced by high surface roughness is believed to increase transmittance and is enough to compensate for the loss caused by grain-boundary scattering. Moreover, the band gap edge for oxygen-deficient films show an obvious shift toward higher wavelength, which is also observed by previous reports[18] and can be ascribed to oxygen-vacancy induced valence band tailing. The haze factors at 360 nm for different films are listed in Table 1. The highest haze factor (35.0% at 360 nm) of the AZO-800 film indicates its quite high surface texture, which well accords with the AFM and SEM results.

The electrical properties of the AZO films are listed in Table 1. The oxygen-deficient AZO films exhibit higher carrier concentration and lower hall mobility than the AZO. The free carrier concentrations (labeled as N in Table 1) of the AZO films are 5.2×10^{20} cm^{-3} (AZO-0), 6.3×10^{20} cm^{-3} (AZO-800), and 8.8×10^{20} cm^{-3} (AZO-900), exhibiting an increasing trend with the increasing post-annealing temperature. The relatively higher carrier concentrations of the oxygen-deficient AZO films are ascribed to the higher concentration of oxygen vacancies in the films, which originate from the as-sputtered targets. However, the carrier concentration of AZO-1000 film separates from the increasing trend, which is attributed to the significant volatility of ZnO at 1000 °C.

The carrier mobility (labeled as μ in Table 1) of the AZO films decreases from 28.3 cm^2/Vs (AZO-0) to 8.3 cm^2/Vs (AZO-1000). Carrier mobility can be affected by grain-boundary scattering and electron carrier scattering, but grain-boundary scattering in AZO polycrystalline film is considered the dominant mechanism[19–21]. The grain-boundary barrier model assumes donor-like positively charged defects in the depletion layer and acceptor-like negatively charged defects in the grain–boundary interface[17,22,23]. The positively charged defects (including trivalent aluminum ions and native oxygen vacancies) extend from both sides of the grain boundary into the adjacent grains and form a positive depletion layer penetrating some distance into the grains. These defects are capable of trapping carriers, thereby immobilizing them and reducing the amount of free carriers.

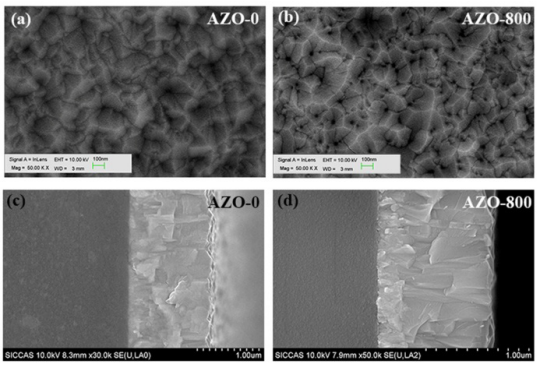

Fig. 4. FE-SEM images for the surface of (a) AZO-0, (b) AZO-800 and cross-section of (c) AZO-0, (d) AZO-800.

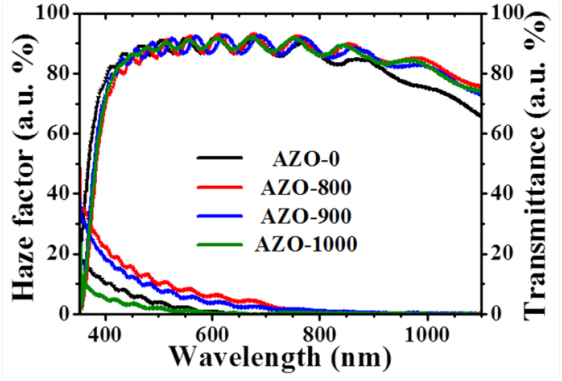

Fig. 5. Transmittance and haze factor spectra of the AZO films.

After trapping the mobile carriers, the traps become electrically charged and create a potential energy barrier to impede the motion of carriers from one crystallite to another and reduce their mobility. The XRD results shown in Fig. 1 reveal that the oxygen-deficient AZO films possess more defects (poorer crystallinity), which are consistent with its much lower mobility.

The resistivity depends on both carrier concentration and carrier mobility. As shown in Table 1, the increased resistivity of the AZO-1000 film is mainly ascribed to the sharply decreased carrier mobility from 28.3 to 8.3 cm^2/Vs. The AZO-800 film balances these two physical components and reaches the lowest resistivity of 4.4×10^{-4} Ω cm.

To examine the performance of our oxygen-deficient AZO film in transparent electrode applications, AZO films (800 nm) deposited by as-sintered target and 800 °C-annealed target were applied as the front contact layer of the CIGS thin film solar cell (labeled as SC-0 and SC-800). The *I-V* characteristic of the fabricated 0.5 × 0.8 (cm) CIGS solar cell under AM 1.5 G simulated solar illumination (100 mW/cm^2) is shown in Fig. 6. The SC-800 cell reaches a higher photocurrent density of 35.71 mA/cm^2, which should be attributed to the lower resistivity of the AZO-800 film. The fill factor also increases from 66.32% (SC-0) to 68.40% (SC-800), and the as-fabricated CIGS solar cell without an antireflective film obtained an optimized efficiency of 14.15%. This result confirms that our oxygen-deficient AZO film improves the performance of CIGS solar cell through improving light transmittance and conductivity, which is identical with the previous reports[24].

In conclusion, highly textured and conducting AZO films are deposited by one-step magnetron sputtering method at room temperature, using the oxygen-deficient targets fabricated via a double-crucible process. For oxygen-deficient AZO film, higher carrier concentration is obtained due to more oxygen vacancy sites compared with the conventional AZO film. The average transmittance exceeds 85% in the wavelength region of 400—1100 nm. The AZO-800 film possesses the highest haze factor of 35.0%, the largest RMS roughness of 18.3 nm, and the lowest resistivity of 4.4×10^{-4} Ω cm. The AZO-800 film is also applied as the window layer of the CIGS solar cell, which achieves a high efficiency of 14.15%. The simplicity of the present method and the superior electrical and optical properties of the films may allow highly conductive AZO films to be used in low-cost commercial applications.

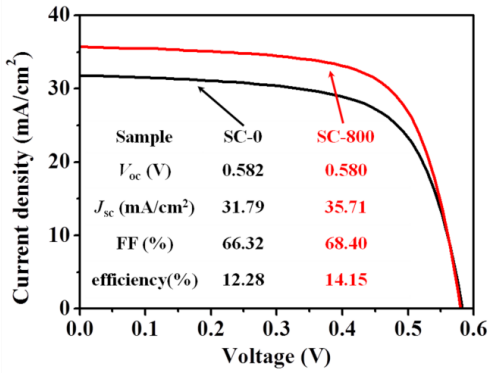

Fig. 6. *I-V* characteristic of CIGS solar cell applying AZO film deposited from as-sintered target (SC-0) and 800 °C-annealed target (SC-800). V_{oc}, open circuit; J_{sc}, short-circuit current; FF, fill factor.

This work was financially supported by the National 863 Program of China (No. 2011AA050505), the National Science Foundation of China (Nos. 51121064 and 51125006), and the Science and Technology Commission of Shanghai (No. 12XD1406800).

References

1. J. G. Mutitu, S. Shi, C. Chen, T. Creazzo, A. Barnett, C. Honsberg, and D. W. Prather, Opt. Express **16,** 15238 (2008).
2. R. G. Gordon, MRS Bull. **25,** 52 (2000).
3. Y. F. Chen, D. M. Bagnall, H. J. Koh, K. T. Park, K. Hiraga, Z. Q. Zhu, and T. Yao, J. Appl. Phys. **84,** 3912 (1998).
4. Y. Hu, Y. Q. Chen, Y. C. Wu, M. J. Wang, G. J. Fang, C. Q. He, and S. J. Wang, Appl. Surf. Sci. **255,** 9279 (2009).
5. J. L. Zhao, X. M. Li, J. M. Bian, W. D. Yu, and C. Y. Zhang, Thin Solid Films **515,** 1763 (2006).
6. K. H. Kim, K. C. Park, and D. Y. Ma, J. Appl. Phys. **81,** 7764 (1997).
7. A. Thankappan, S. Thomas, and V. P. N. Nampoori, Chin. Opt. Lett. **11,** 101801(2013).
8. C. R. Gorla, N. W. Emanetoglu, S. Liang, W. E. Mayo, Y. Lu, M. Wraback, and H. Shen, J. Appl. Phys. **85,** 2595 (1999).
9. E. Gur, S. Tuzemen, K. Meral, and Y. Onganer, Appl. Phys.A: Mater. Sci. Process. **94,** 549 (2009).
10. G. Z. Xing, B. Yao, C. X. Cong, T. Yang, Y. P. Xie, B. H. Li, and D. Z. Shen, J. Alloys Compd. **457,** 36 (2008).
11. G. J. J. Fang, D. J. Li, and B. L. Yao, Thin Solid Films **418,** 156 (2002).
12. R. G. S. Pala and H. Metiu, J. Phys. Chem. C **111,** 12715 (2007).
13. J. Yoo, J. Lee, S. Kim, K. Yoon, I. J. Park, S. K. Dhungel, B. Karunagaran, D. Mangalaraj, and J. S. Yi, Thin Solid Films **480,** 213 (2005).
14. C. Agashe, O. Kluth, G. Schope, H. Siekmann, J. Hupkes, and B. Rech, Thin Solid Films **442,** 167 (2003).
15. C. Yang, D. Wan, Z. Wang, and F. Huang, Chin. Opt. Lett. **9,** 103102 (2011).
16. D. Wan, F. Huang, Y. Wang, X. Mou, and F. Xu, ACS Appl. Mater. Interf. **2,** 2147 (2010).
17. J. Y. W. Seto, J. Appl. Phys. **46,** 5247 (1975).
18. R. Hong, J. Shao, H. He, and Z. Fan, Chin. Opt. Lett. **3,** 428 (2005).
19. J. F. Chang and M. H. Hon, Thin Solid Films **386,** 79 (2001).
20. F. R. Blom, F. C. M. Vandepol, G. Bauhuis, and T. J. A. Popma, Thin Solid Films **204,** 365 (1991).
21. T. Minami, H. Sato, K. Ohashi, T. Tomofuji, and S. Takata, J. Cryst. Growth **117,** 370 (1992).
22. N. S. Choudhury , J. Electrochem. Soc. **120,** 1663 (1973).
23. T. K. Gupta, W. D. Straub, M. S. Ramanachalam, J. P. Schaffer, and A. Rohatgi, J. Appl. Phys. **66,** 6132 (1989).
24. R. Liu, Z. Xia, Y. Wu, H. Jiao, Z. Liang, and J. Zhou, Chin. Opt. Lett. **11,** 120501 (2013).